OPTICA

Stimulated Raman photothermal spectroscopy for gas sensing in a hollow-core optical fiber

Hanyu Liao,[1,2,†] Yan Zhao,[1,2,†] Kaiyuan Zheng,[1,2] Haihong Bao,[1,2] Shoulin Jiang,[1,2] Hoi Lut Ho,[1,2] Shoufei Gao,[3] Yingying Wang,[3] and Wei Jin[1,2,*]

[1]Department of Electrical and Electronic Engineering and Photonics Research Institute, The Hong Kong Polytechnic University, Hung Hom, Kowloon, Hong Kong SAR, China
[2]Photonics Research Center, The Hong Kong Polytechnic University Shenzhen Research Institute, Nanshan District, Shenzhen, China
[3]Institute of Photonics Technology, Jinan University, Guangzhou, China
[†]These authors contributed equally to this work.
*wei.jin@polyu.edu.hk

Received 29 April 2024; revised 24 July 2024; accepted 29 October 2024; published 12 December 2024

Raman spectroscopy is an essential optical tool for tracing gases that exhibit weak or no infrared absorption. Existing Raman spectroscopic methods are deficient for precision sensing applications due to the extremely low Raman cross-section of gas. Herein, we report an approach, named stimulated Raman photothermal spectroscopy (SRPTS), to indirectly probe stimulated Raman scattering (SRS) via detecting the induced photothermal phase modulation in a gas-filled hollow-core fiber (HCF). Photothermal interferometry enables a linear increase of the SRPTS signal with the product of the pump and Stokes power while maintaining low background noise at the idle probe wavelength. The HCF tightly confines the light beams and the gas sample to significantly enhance both the SRS gain and the photothermal phase modulation efficiency. Preliminary experimentation with a 3.9-m-long HCF demonstrates hydrogen detection with a noise equivalent concentration of 6.8 ppm (parts-per-million) under 100 s averaging time and 6 bar gas pressure, indicating the potential for high-precision gas detection in chemical, medical, and energy industries.

https://doi.org/10.1364/OPTICA.528840

1. INTRODUCTION

Trace gas detection has great importance in environmental monitoring, medical breath analysis, industrial process control, and security applications [1,2]. Among the various gas sensing methods, infrared spectroscopy based on light absorption associated with rovibrational transitions offers outstanding advantages in selectivity and sensitivity [3,4]. Infrared spectroscopy is typically implemented by detecting the change of transmitted light intensity as exemplified by diode laser absorption spectroscopy (TDLAS) [5] and cavity-enhanced absorption spectroscopy (CEAS) [6], or the subsequent effects of optical absorption such as photoacoustic spectroscopy (PAS) [7] and photothermal spectroscopy (PTS) [8]. However, for homo-nuclear diatomic gases, molecular vibrations do not induce a change in the dipole moment and hence no strong coupling to the infrared radiation. Infrared spectroscopy may still be employed on the vibration-induced change in the quadrupole moment; however, the detection sensitivity is much limited by the weak quadrupole transition, which is inherently five to six orders of magnitude smaller than that of the dipole transition [9,10].

Raman spectroscopy is an alternative method to infrared spectroscopy, particularly viable for tracing infrared-inactive gases. Despite its potential, the technique faces challenges in achieving high-precision detection of gases due to the weak Raman scattering cross-sections of gas molecules. To overcome this limitation, various efforts have been made to improve the efficiency of Raman scattering, such as cavity-enhanced Raman spectroscopy (CERS) [11,12] and coherent anti-Stokes Raman spectroscopy (CARS) [13,14]. By using micro/nano-structured optical fibers to confine light fields tightly within the gas medium, significant enhancement of stimulated Raman scattering (SRS) and signal collection efficiencies are achieved at ambient conditions [15–19]. Indirect measurement of the photoacoustic effect induced by the SRS (PARS) has also been reported with a decent detection limit of down to 40 ppm for hydrogen [20–22]. PARS requires highly sensitive microphones, which are mostly non-optical and detect only the local pressure change on a limited sensing area (e.g., mm to cm in diameter). The sensitivity of the PARS would not be significantly improved by simply increasing the length of the gas cell [20,23].

Here, we demonstrate that the SRS process of gas molecules induces a photothermal phase modulation, and the modulation efficiency can be enhanced by more than four orders of magnitude using anti-resonant hollow-core fiber (AR-HCF) as compared to free-space counterparts. We then introduce a novel approach to gas (hydrogen) sensing by measuring this phase modulation in AR-HCF, which is named stimulated Raman photothermal spectroscopy (SRPTS). The energy of the SRS pump field is transferred to the Stokes field and vibrating molecules, where the

2334-2536/24/121682-08 Journal © 2024 Optica Publishing Group

latter subsequently dissipates as localized heating in the hollow core through molecule relaxation. The temperature change in the fiber core is indirectly measured by detecting the phase difference between the two optical modes in the AR-HCF at the probe wavelength. The AR-HCF offers high optical mode field intensity, fast thermal conductivity, long interaction distance, low nonlinear background, and nearly 100% overlap between the optical fields and gas sample [24,25]. The broad transmission window of the AR-HCF, covering the widely separated pump and Stokes wavelengths, enables the excitation of the vibrational Raman transition of hydrogen and hence greatly improves the heat generation efficiency and the resulting phase modulation. In virtue of this powerful method, we have realized state-of-the-art hydrogen sensing with ppm level sensitivity in a meter-long HCF gas cell.

2. PRINCIPLE OF SRPTS IN HCF

A. Heat Generation in SRS

SRS involves two laser beams: a pump beam and a downshift Stokes beam. Taking the $Q_1(1)$ vibrational transition of hydrogen as an example, when the frequency difference between the pump (ν_P) and Stokes (ν_s) matches the Raman frequency shift (ν_R), a pump photon is converted to a Stokes photon, and the molecule is excited to an upper vibrational energy level. The excited molecule would return to the ground vibrational state via thermal relaxation. As illustrated in Fig. 1(a), from the perspective of SRPTS, part of the pump energy is converted to heat by SRS with an energy efficiency of ν_R/ν_P. The generated heat serves as a source to change the temperature of the gas sample, which may be expressed as (Supplement 1, S1):

$$Q = P_P P_S |\psi_P \psi_S|^2 g_R \frac{\nu_R}{\nu_P}, \tag{1}$$

where $P_{P,S}$ and $\psi_{P,S}$ are, respectively, the optical power and normalized mode field distribution of the pump and Stokes beams, and g_R is the Raman gain. According to Eq. (1), the heat generation depends on the Raman gain (g_R) and the Raman frequency shift (ν_R) of the selected Raman line, for which the vibrational Raman transition would be much more efficient than the rotational Raman transition. Tight confinement of the pump and Stokes modes ($|\psi_P \psi_S|^2$) also significantly improves the heat generation efficiency.

B. Heat Transfer in HCF

SRPTS detects the heating-induced phase change of another light beam (probe) in the AR-HCF. The HCF acts as a highly efficient platform for both SRS [24] and photothermal phase modulation [26,27]. The heat conduction of the silica structure in HCF extends the thermal response to tens of kilohertz, allowing us to apply the wavelength modulation technique on the Stokes laser to reduce the detected noise [27]. The AR-HCF used in our experiment supports primarily two optical modes (i.e., LP_{01}-like and LP_{11}-like modes) to form a dual-mode interferometer (DMI), which measures the temperature change through mode-phase-difference. This simple in-line interferometer has demonstrated excellent performance in minimizing the effect of external disturbance on gas detection based on PTS [28]. The property of the HCF and implementation of the DMI can be found in Supplement 1, S2.

Ideally, the pump and Stokes beams can be perfectly coupled into the fundamental LP_{01} mode of the HCF, where only the intra-mode SRS needs to be considered. The corresponding SRS

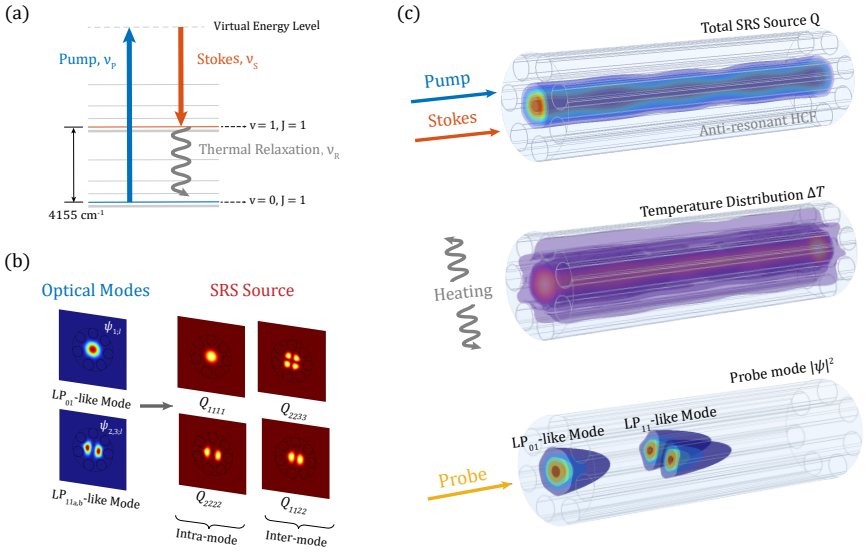

Fig. 1. Principle of photothermal spectroscopy based on SRS. (a) Energy diagram of hydrogen vibrational SRS. Part of the energy of the pump photon is transferred to the heat with an energy efficiency of ν_R/ν_P. (b) The multi-mode SRS inside the HCF. The electric fields of the three optical modes ($\psi_{i;l}$) contribute to forming the SRS sources ($Q_{\sigma\upsilon\zeta\eta}$). The index $i = 1, 2, 3$ refers to the LP_{01} mode, LP_{11a} mode, and LP_{11b} mode, respectively; the index $l = 0, 1$ refers to the pump and Stokes frequency, respectively. $Q_{\sigma\upsilon\zeta\eta}$ defines the heat source induced by SRS from the pump mode η to the Stokes mode σ due to the molecule coherent wave generated by pump mode ζ and Stokes mode υ. (c) Illustration of SRPTS in an HCF. Pump, Stokes, and probe beams co-propagate along the HCF; the multi-mode SRS results in heat generation, which changes the temperature distribution and hence the phase of the two probe modes. The pump and Stokes power is assumed to be 200 mW with Stokes wavelength modulation at 6 kHz. The HCF is filled with 100 ppm hydrogen under 6 bar gas pressure. The mode power fraction is determined by the experiment with $\mu_{1;l} = 3\mu_{2,3;l}$. The HCF plotted here is 4.5 mm long.

heat source (Q_{1111}) is of Gaussian-like profile, which is described as $\psi_1^*\psi_1\psi_1^*\psi_1$ in Eq. (1). In practice, the few-mode nature of the HCF leads to a complex distribution of the SRS heat sources in the hollow core of the fiber. As shown in Fig. 1(b), there are two kinds of mode heat sources generated by SRS: the heat sources due to intra-modal SRS and the heat sources due to inter-modal SRS. The upper panel in Fig. 1(c) shows the sum of these heat sources along the HCF. The beat pattern is due to the interference of optical modes, and for the AR-HCF used here, the modal beat lengths are about 3.2 mm and 1.7 mm for the pump beam and Stokes beam, respectively. Due to the wavelength modulation on the Stokes beam, the heat sources are time-periodic, leading to a modulation of the temperature distribution in HCF through thermal conduction. The amplitude of the time-oscillating temperature distribution (ΔT) is drawn in the middle panel of Fig. 1(c), and the periodic fluctuation along the fiber is caused by the phase unmatched inter-modal SRS heat sources (Supplement 1, S3).

C. Probe the Heating-Induced Phase Change

The temperature change due to the SRS heat source is measured by the phase difference between the LP_{01} mode and LP_{11a} (or LP_{11b}) mode of the probe beam, as shown in the lower panel of Fig. 1(c). The change of the mode-phase-difference of the probe beam due to the Raman photothermal (RPT) process may be expressed as (detailed theory in Supplement 1, S3)

$$\Delta\phi = \Delta\phi_{01} - \Delta\phi_{11} = k_R^*(\mu_{P,S}, \omega_{eff}, f, n, \nu_L, p) P_P P_S g_R L$$
$$\propto (n-1)\nu_L \nu_R \frac{g_R}{\nu_P} \frac{P_P P_S L}{w_{\text{eff}}^4}, \tag{2}$$

where $\mu_{P,S}$ is the fractional mode power of the pump and Stokes beams in the hollow core, L the length of HCF, w_{eff} the effective mode field radius, and k_R^* the RPT phase modulation coefficient. k_R^* depends on the fractional mode power of the pump and Stokes ($\mu_{P,S}$), the effective mode radius (w_{eff}), the modulation frequency of the pump or Stokes laser (f), the refractive index of gas (n), the probe wavenumber (ν_L), and the gas pressure (p) in the hollow core. The use of HCF greatly improves the efficiency of RPT by tightly confining the optical fields inside a small hollow core over a long distance, as described by the factor L/w_{eff}^4. Compared with the free-space Gaussian beam, the RPT phase modulation in HCF could be 10,000 times larger owing to a much higher nonlinear SRS efficiency [24] and photothermal phase modulation efficiency [27]. The indirect measurement of SRS by its photothermal effect also enables the use of a higher power pump and Stokes beam ($P_{P,S}$) while the noise floor of the idle probe beam remains unchanged, for which the signal-to-noise ratio (SNR) increases linearly with the power product of the pump and Stokes beams. For SRPTS, the heat generated by SRS is proportional to the Raman frequency shift (ν_R). Taking hydrogen as an example, the Raman frequency shift of the $Q_1(1)$ vibrational transition and the $S_0(0)$ rotational transition are 4155 cm^{-1} and 354 cm^{-1}, respectively; furthermore, the SRS gain of $Q_1(1)$ transition and the factor $(n-1)$ in Eq. (1) would increase greatly with higher gas pressure. For this reason, we select the $Q_1(1)$ transition of hydrogen with 6 bar pressure for the experiment, where the RPT phase modulation would be 455 times larger than that of the $S_0(0)$ transition of unpressurized hydrogen.

3. EXPERIMENTS AND RESULTS

A. Experiment Setup

The experiment setup is shown in Fig. 2. The Raman heating is generated by two lasers: an external cavity diode laser (ECDL, the pump) around 940 nm and a distributed feedback (DFB) laser (the Stokes) around 1542 nm. The wavenumber difference between the two lasers corresponds to the $Q_1(1)$ vibrational Raman transition at $\nu_R = 4155\ \text{cm}^{-1}$. The wavelength of the Stokes laser is sinusoidally modulated by current modulation via the internal signal generator of a lock-in amplifier and simultaneously sweeps slowly across the Raman transition line by temperature tuning with a triangular waveform. The power of the Stokes laser is amplified by an erbium-doped fiber amplifier (EDFA). The probe beam is from a 1550 nm fiber laser and coupled to the HCF with offset alignment, by which the LP_{01} mode and LP_{11} mode are excited simultaneously to form a DMI. The wavelength of the probe laser can be tuned by the built-in piezoelectric transducer (PZT) of the laser with a feedback loop to lock the DMI to quadrature. The Stokes is first combined with the probe by using a wavelength division multiplexer (WDM) and then combined with the pump using a dichroic mirror (DM). Two lenses are used for coupling light into the AR-HCF and collecting light from it with a coupling loss of ~3 dB. The HCF gas cell is made of two homemade aluminum chambers and a 3.9-m-long AR-HCF, and the propagation loss for the pump and Stokes beams is 1.2 dB/m and 1.8 dB/m, respectively. The test gas is pressurized into the AR-HCF from both ends, and the gas filling time can be less than 30 s when the gas pressure is above 5 bar. A balance photodetector (BPD) is used to detect the probe light from the DMI. The SRPTS signal is analyzed by the lock-in amplifier (LIA), and the 2nd harmonic is used as the output signal.

B. Characterization of SRPTS

We first measured the frequency response of the SRPTS signal in the 3.9-m-long HCF gas cell filled with 1% hydrogen balanced with nitrogen at a gas pressure of 6 bar. The powers of the pump and Stokes inside the HCF are measured to be 277 mW and 250 mW at the output end of the HCF, respectively. Figure 3(a) shows the 2nd harmonic SRPTS signal from the LIA when the modulation frequency of the Stokes is varied from 100 Hz to 80 kHz. The SRPTS signal reaches a peak at 1 kHz and then decreases, whereas the measurement error in terms of s.d. of signal fluctuation becomes smaller with increasing modulation frequency. We simulate the frequency response of the SRPTS signal caused by the multi-mode SRS source, and the normalized SRPTS phase modulation coefficients of different mode heat sources, i.e., Q_{1111}, Q_{1122}, Q_{2222}, and Q_{2233}, are shown in Fig. 3(b). The mode heat sources related to LP_{11}-like modes (i.e., $\psi_{2;l}$) all present a peak phase modulation coefficient around 1–4 kHz, which agrees with the experiment results. To explain the dependence of RPT phase modulation on modulation frequency, we take the Q_{1122} component, the most powerful heat source except Q_{1111} in our experiment as an example, and the corresponding isotherm is drawn in the insets of Fig. 3(b). Initially, the temperature change (ΔT) exhibits a Gaussian-like profile, which has a larger overlap with probe LP_{01} mode than LP_{11} mode. This leads to a high and positive mode-phase-difference ($\Delta\phi_{01} - \Delta\phi_{11}$), peaking at 1 kHz where the alignment to the LP_{01} mode is the closest. As the modulation frequency increases, the temperature response becomes less

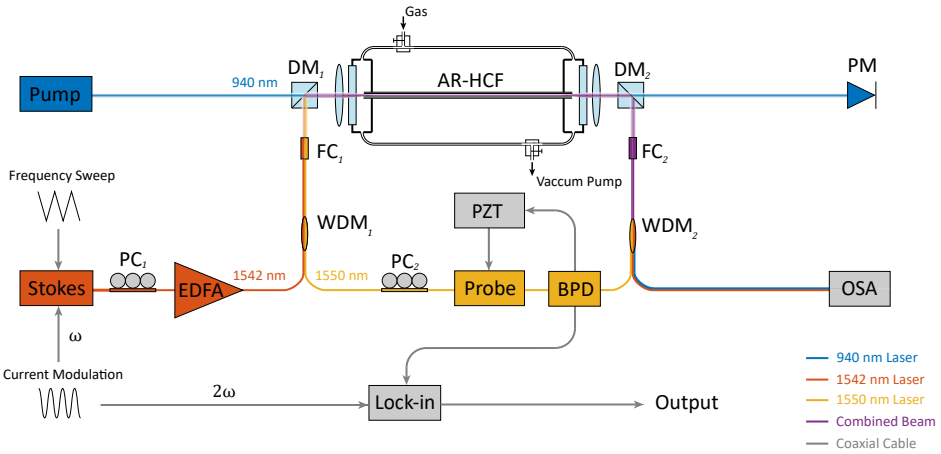

Fig. 2. The experimental setup. PC: polarization controller; EDFA: erbium-doped fiber amplifier; WDM: wavelength division multiplexer; FC: fiber-pigtailed collimator; DM: dichroic mirror; PM: power meter, to monitor the pump power in the HCF; OSA: optical spectrum analyzer; PZT: piezoelectric transducer; BPD: balanced photodetector.

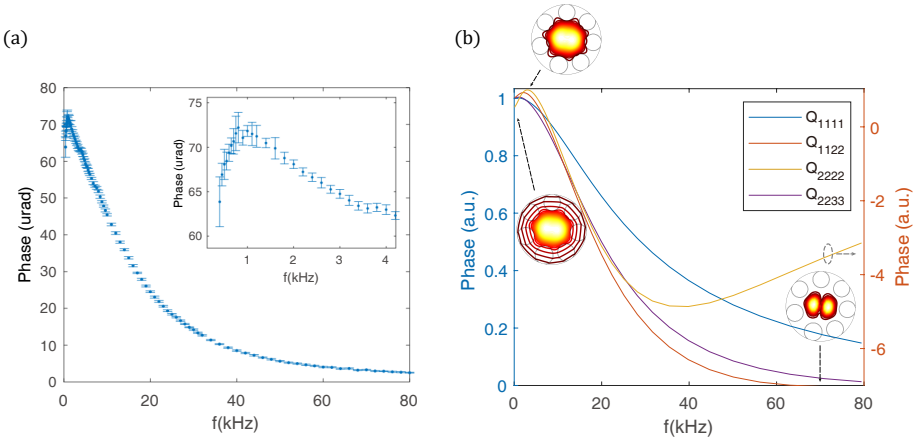

Fig. 3. Frequency response of SRPTS. (a) The measured 2nd harmonic phase modulation at different demodulation frequencies. The error bar shows the s.d. from 5 times measurements. (b) Simulated frequency response for different SRS mode heat sources. The three insets are the isotherm corresponding to Q_{1122} heat source at modulation frequencies of 100 Hz, 1 kHz, and 70 kHz, respectively, which shows the profile of the temperature distribution $\Delta T(r, \theta)$. The right axis shows the frequency response for Q_{2222}, which changes most rapidly from positive to negative (Supplement 1, Section 3).

effective due to the lower heat conduction rate of air, resulting in a reduced and more localized isotherm, which has a larger overlap with the LP_{11} mode. Consequently, the mode-phase-difference decreases or even inverts. The same reasoning applies to the other heat sources. The linear superposition of all the mode heat sources constructs the total SRS heat source in our experiments. The corresponding 3 dB roll-off frequency of SRPTS with hydrogen is about 14 kHz, which indicates that the vibrational relaxation time of hydrogen is significantly larger than acetylene, which is ~40 kHz [26].

We then test the performance of SRPTS under different gas pressures with the modulation frequency fixed at 3 kHz. Figure 4(a) shows the 2nd harmonic LIA output when the Stokes laser is tuned across the $Q_1(1)$ Raman transition of hydrogen for different gas pressures. It is observed that the SRPTS has a quadratic relationship with pressure near 1–4 bar, as shown in Fig. 4(b). This quadratic relationship is mainly due to the Dicke narrowing effect [29], which increases the SRS gain (g_R) due to the reducing linewidth (Supplement 1, S1). For gas pressure higher than 6 bar, the SRS gain tends to saturate due to the collisional broadening, and the SRPTS signal increases approximately linearly with the gas pressure. We also conduct experiments where the gas sample is pressurized into the HCF solely from the gas inlet, leaving the outlet open to the air. The SRPTS signal decreases to 74% of the original value, which is primarily due to the non-uniform pressure distribution along the HCF.

C. Detection Limit of SRPTS

The power dependence of the SRPTS signal is investigated with the modulation frequency fixed at 3 kHz and the gas pressure at 6 bar. Figures 5(a) and 5(c) show the 2nd harmonic LIA output when the Stokes laser is tuned across the $Q_1(1)$ Raman transition of hydrogen for different pump and Stokes power levels. For a fixed pump (Stokes) power, the amplitude of the SRPTS signal shows a linear dependence on the Stokes (pump) power, as demonstrated in Figs. 5(b) and 5(d). The 2nd harmonic signal of SRPTS shows a linear dependence on the product of the pump and Stokes powers while the standard deviation (s.d.) of the detected noise remains almost unchanged, as shown in Fig. 6(a). The SRPTS accordingly allows us to improve the signal-to-noise ratio (SNR) by simply increasing the pump and Stokes powers.

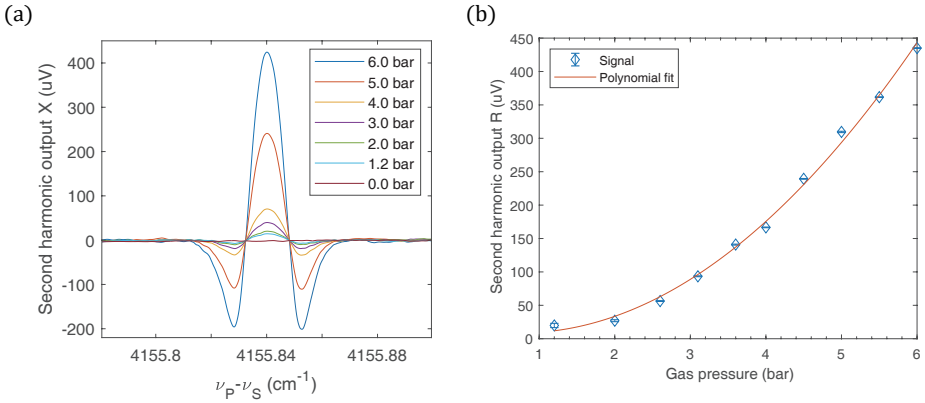

Fig. 4. Pressure dependence of SRPTS. (a) The 2nd harmonic X-output of LIA under different gas pressures for 1% hydrogen balanced with nitrogen. (b) The pressure dependence of the amplitude of 2nd harmonic output of LIA. The error bar shows the s.d. of the signal from 5 times measurements with the time constant of the LIA set to 1 s. The red curve is the 2-order polynomial fit.

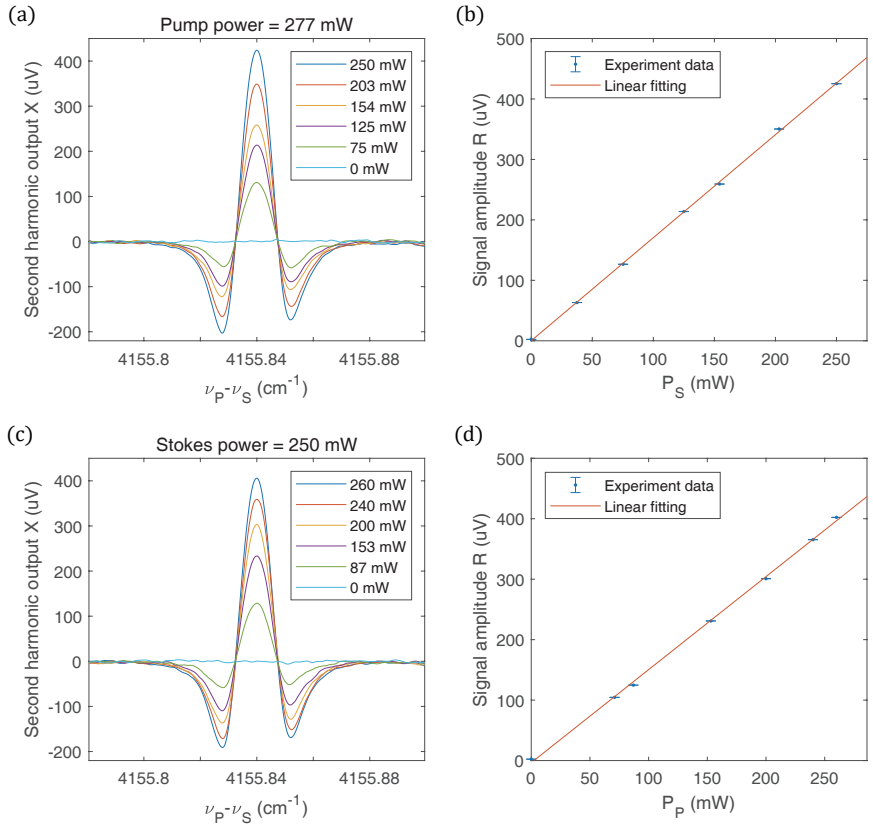

Fig. 5. Results of pump and Stokes power dependence. (a) The 2nd harmonic output of LIA with different Stokes powers. (b) The Stokes power dependence of the amplitude of 2nd harmonic output of LIA. (c) The 2nd harmonic output of LIA with different pump powers. (d) The pump power dependence of the amplitude of 2nd harmonic output of LIA. The LIA time constant is 1 s with 18 dB Oct^{-1}, corresponding to 0.094 Hz detection bandwidth. The "X" and "R" refer to the X-output and R-output of the LIA, respectively.

The noise of the system is evaluated by detuning the wavelength of Stokes away from the Raman transition with the time constant of the LIA set to 1 s. At the pump and Stokes power of 277 mW and 250 mW, respectively, the standard deviation of the noise is 896 nV. The amplitude of the 2nd harmonic signal for 1% of hydrogen is 424 μV, giving an SNR of 473 and a noise equivalent concentration (NEC) of 21 ppm. It is shown that the second harmonic amplitude is linearly proportional to the hydrogen concentration in the range of 0–2%; hence, the NECs estimated under different hydrogen concentrations are approximately the same (Supplement 1, S4). To further investigate the sensitivity of the SRPTS, Allan-Werle analysis is conducted with the noise data recorded for more than 10 h with a lock-time constant of 100 ms. As depicted in Fig. 6(b), the system noise is dominated by white noise at shorter integration times and changes to random walk noise for integration times larger than 1000 s [30]. For an averaging time of ∼100 s, the SNR is 1460, giving a detection limit of 6.8 ppm hydrogen. The NEC of our system is about 3.2 ppm hydrogen with an integration time of 1627 s.

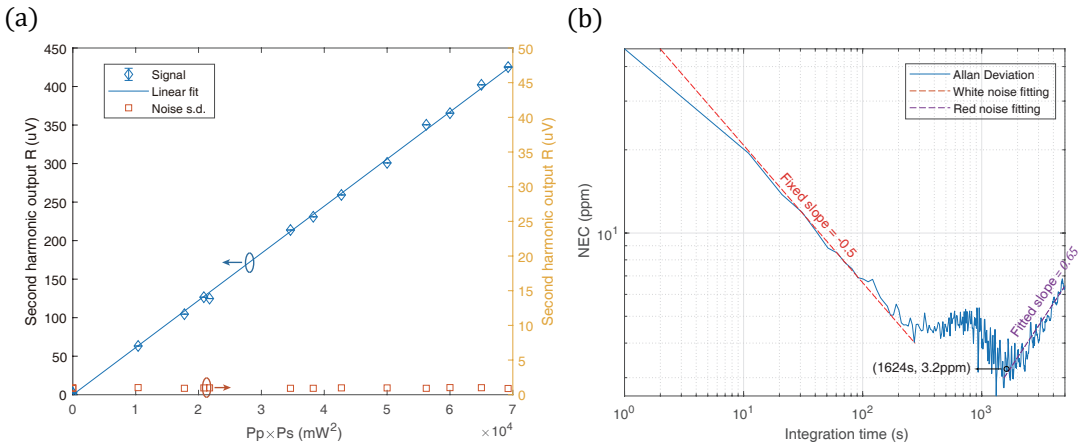

Fig. 6. Results of SNR analysis. (a) The signal and noise of 2nd harmonic R-output of LIA with different products of pump and Stokes powers for 1% hydrogen balanced with nitrogen. The error bar for the blue line shows the s.d. from 5 times measurements. The red points show the s.d. of the noise, which is nearly unchanged with pump and Stokes power. (b) The Allan-Werle analysis based on the measured data over 10 h. The fitted drift gradient is 0.65, where the random walk noise dominates the NEC. The optimal SNR is achieved for 1627 s integration time.

4. DISCUSSION

In conclusion, a new spectroscopic sensing method based on the photothermal effect associated with SRS is demonstrated with an AR-HCF and achieved, in a preliminary experiment, a sensitivity of 6.8 ppm for hydrogen detection with ∼100 s averaging time and 6 bar pressure, which is comparable to state-of-the-art hydrogen sensors, as listed in Table 1. The high sensitivity is attributed to the indirect measurement of SRS, which obviates the need for accurate detection of small changes in laser irradiance due to the SRS gain or loss. Compared with other spectroscopy methods, SRPTS has a distinct affinity in the application of optical fiber systems. The broadband transmission window of HCF, along with its superior confinement of both the optical mode and gas sample, significantly improves the performance of SRPTS and makes it particularly promising for sensing applications. There is a wide room for employing optical phase amplification techniques [38,39] and matured infrared fiber-optic components to make compact and cost-effective sensors based on SRPTS with high selectivity and sensitivity.

The SRPTS we reported here has unique characteristics that can be utilized for further improvement. First, since both the SRS and the photothermal phase modulation benefit from high optical intensity, the RPT phase modulation shows exceptional dependence on the fourth power of the effective mode radius, as described by the factor w_{eff}^{-4} in Eq. (2). By using specially designed or down-tapered HCF with a much-reduced mode field area [40], the sensitivity of the SRPTS can be significantly enhanced. For example, if we could down-taper the HCF to reduce the diameter of the fiber by a quarter, the SRPTS signal would increase by 256 times. Second, different SRS mode heat sources have different phase modulation to the probe modes. The RPT phase modulation coefficient k_R^* could be increased several times by carefully choosing the excited modes of the pump and Stokes beams for a highly efficient SRS heat source [41]. Third, the SRPTS could operate at shorter pump wavelengths, which may further increase the SRS gain and hence the detection sensitivity. In addition, SRPTS can be performed in a pulse format for much higher peak optical power, where the SRS and also photothermal phase modulation increase with decreasing pulse duration [42]. For example, if we apply 1 μJ

Table 1. Comparison of Optical Techniques for Hydrogen Sensing[a]

Techniques	Mechanisms	Sensing Elements	LLD (ppm)	Response Time
MZ [31]	Interaction with coating	6 cm Pd-coated SMF	2	<8 min
SPR [32]	Interaction with coating	1.5 cm Pd-coated MMF	8×10^3	<5 min
TLSRS [33]	Thermal-lens effect	40 cm thermal-lens tube	9	N.A.
PARS [22]	Photoacoustic effect of SRS	14 cm acoustic tube	4.6	N.A.
FERS [34]	HCF-enhanced SR	1 m HC-580-02 fiber	4.7	<3 min
SRGS [35]	WMS of SRS	15 m HC-1550-02 fiber	17	<4 h
NFSRS [18]	NF-enhanced WMS of SRS	4.8 cm silica nanofiber	3	<10 s.
LAS [36]	WMS of quadrupole absorption	10.13 m optical length HPMC	522	N.A.
CERS [11]	Cavity-enhanced SR	35 cm high-finesse free-space cavity	460	N.A.
CARS [37]	Intra-cavity CARS	25 cm high-finesse free-space cavity	N.G.	N.A.
This Work	Photothermal WMS of SRS	3.9 m HC-1550-02 fiber	6.8	<30 s

[a]LLD: lower limit of detection; MZ, Mach–Zehnder interferometer; SPR, surface plasma resonance; TLSRS, thermal-lens stimulated Raman spectroscopy; PARS, photoacoustic Raman spectroscopy; FERS, fiber-enhanced Raman spectroscopy; SRGS, stimulated Raman gain spectroscopy; NFSRS, nanofiber-enhanced stimulated Raman spectroscopy; LAS, laser absorption spectroscopy; CERS, cavity-enhanced Raman spectroscopy; CARS, coherent anti-Stokes Raman spectroscopy; SR, spontaneous Raman; WMS, wavelength modulation spectroscopy; NF, nanofiber; SMF, single mode fiber; MMF, multi-mode fiber; HPMC, Herriott multipass gas cell. N.G., not given/determined. N.A., not applicable.

pump pulse and Stokes pulse with a 10 ns width and 3 kHz repetition rate, the corresponding RPT phase modulation could reach 1.04 mrad, which is 20 times larger than the phase modulation measured in our experiment.

The sensitivity of SRPTS can also be enhanced by directly using high-power pump and Stokes beams, since the noise level stays unchanged with increasing pump and Stokes power. For HCF, the minimal overlap between the fiber material and the mode fields allows for the transmission of laser beams with average power levels up to 70 W [43]. There is plenty of room for the use of optical amplifiers and high-power lasers, and even sub-ppm level hydrogen detection could be possible. However, in high optical power scenarios, it may be necessary to consider the issue of other relaxation pathways that compete with the collision and lower the RPT strength. In our configuration, these effects can be safely neglected if the pump and Stokes powers are less than 10 W (Supplement 1, S5).

The SRPTS holds great promise for applications on nanoplatforms such as optical nanofiber and on-chip waveguides, which have a much tighter mode field and higher thermo-optic phase modulation efficiency [44,45]. SRPTS can also be combined with other Raman-enhancing techniques such as Resonance Raman spectroscopy [46] and surface-enhanced Raman spectroscopy [47] for orders of magnitude higher Raman scattering cross-section. By designing microstructured waveguides with broader transmission bands, Raman transitions with higher Raman frequency shifts could be utilized to further improve the sensitivity of SRPTS. The technique could be similarly extended to trace other gases, chemicals, and liquids.

Funding. The Hong Kong SAR government (GRF grant (15206523)); Hong Kong Polytechnic University (1-ZVY4, 1-W24Q, 1-W229, 1-W32D); The Hong Kong Polytechnic University Shenzhen Research Institute (P0039515).

Acknowledgment. Y. Z. and H. L. built the systems and conducted the experiments. K. Z. and H. B. assisted in building the systems and conducting the experiments. Y. Z. and H. L. developed the mathematical formulations. H. L. performed the numerical modeling and analyzed the results. Y. Z., K. Z., H. B., and S. J. assisted in analyzing the results. H. L., Y. Z., W. J., and K. Z. prepared the manuscript. S. G. and Y. W. designed and fabricated the AR-HCF. W. J. conceived the idea of SRPTS and coordinated the project.

Disclosures. The authors declare no conflicts of interest.

Data availability. Data underlying the results presented in this paper are available in Zenodo [48].

Supplemental document. See Supplement 1 for supporting content.

REFERENCES

1. P. A. Martin, "Near-infrared diode laser spectroscopy in chemical process and environmental air monitoring," Chem. Soc. Rev. **31**, 201–210 (2002).
2. U. Willer, M. Saraji, A. Khorsandi, *et al.*, "Near-and mid-infrared laser monitoring of industrial processes, environment and security applications," Opt. Laser Eng. **44**, 699–710 (2006).
3. P. Werle, F. Slemr, K. Maurer, *et al.*, "Near-and mid-infrared laser-optical sensors for gas analysis," Opt. Laser Eng. **37**, 101–114 (2002).
4. J. Hodgkinson and R. P. Tatam, "Optical gas sensing: a review," Meas. Sci. Technol. **24**, 012004 (2012).
5. P. Werle, R. Mücke, and F. Slemr, "The limits of signal averaging in atmospheric trace-gas monitoring by tunable diode-laser absorption spectroscopy (TDLAS)," Appl. Phys. B **57**, 131–139 (1993).
6. J. Ye, L.-S. Ma, and J. L. Hall, "Ultrasensitive detections in atomic and molecular physics: demonstration in molecular overtone spectroscopy," J. Opt. Soc. Am. B **15**, 6–15 (1998).
7. F. J. Harren, G. Cotti, J. Oomens, *et al.*, "Photoacoustic spectroscopy in trace gas monitoring," Encyclopedia Anal. Chem. **3**, 2203–2226 (2000).
8. S. E. Bialkowski, *Photothermal Spectroscopy Methods for Chemical Analysis* (Wiley, 1996).
9. V. Avetisov, O. Bjoroey, J. Wang, *et al.*, "Hydrogen sensor based on tunable diode laser absorption spectroscopy," Sensors **19**, 5313 (2019).
10. U. Fink, T. Wiggins, and D. Rank, "Frequency and intensity measurements on the quadrupole spectrum of molecular hydrogen," J. Mol. Spectrosc. **18**, 384–395 (1965).
11. R. Salter, J. Chu, and M. Hippler, "Cavity-enhanced Raman spectroscopy with optical feedback cw diode lasers for gas phase analysis and spectroscopy," Analyst **137**, 4669–4676 (2012).
12. M. Hippler, "Cavity-enhanced Raman spectroscopy of natural gas with optical feedback cw-diode lasers," Anal. Chem. **87**, 7803–7809 (2015).
13. R. Begley, A. Harvey, and R. L. Byer, "Coherent anti-Stokes Raman spectroscopy," Appl. Phys. Lett. **25**, 387–390 (1974).
14. W. M. Tolles, J. W. Nibler, J. McDonald, *et al.*, "A review of the theory and application of coherent anti-Stokes Raman spectroscopy (CARS)," Appl. Spectrosc. **31**, 253–271 (1977).
15. M. P. Buric, K. P. Chen, J. Falk, *et al.*, "Enhanced spontaneous Raman scattering and gas composition analysis using a photonic crystal fiber," Appl. Opt. **47**, 4255–4261 (2008).
16. J. L. Doménech and M. Cueto, "Sensitivity enhancement in high resolution stimulated Raman spectroscopy of gases with hollow-core photonic crystal fibers," Opt. Lett. **38**, 4074–4077 (2013).
17. P. G. Westergaard, M. Lassen, and J. C. Petersen, "Differential high-resolution stimulated CW Raman spectroscopy of hydrogen in a hollow-core fiber," Opt. Express **23**, 16320–16328 (2015).
18. Y. Qi, Y. Zhao, H. Bao, *et al.*, "Nanofiber enhanced stimulated Raman spectroscopy for ultra-fast, ultra-sensitive hydrogen detection with ultra-wide dynamic range," Optica **6**, 570–576 (2019).
19. S. Hanf, R. Keiner, D. Yan, *et al.*, "Fiber-enhanced Raman multigas spectroscopy: a versatile tool for environmental gas sensing and breath analysis," Anal. Chem. **86**, 5278–5285 (2014).
20. J. Barrett and D. Heller, "Theoretical analysis of photoacoustic Raman spectroscopy," J. Opt. Soc. Am. **71**, 1299–1308 (1981).
21. G. A. West and J. J. Barrett, "Pure rotational stimulated Raman photoacoustic spectroscopy," Opt. Lett. **4**, 395–397 (1979).
22. C. L. Spencer, V. Watson, and M. Hippler, "Trace gas detection of molecular hydrogen H2 by photoacoustic stimulated Raman spectroscopy (PARS)," Analyst **137**, 1384–1388 (2012).
23. O. Kilic, M. Digonnet, G. Kino, *et al.*, "External fibre Fabry–Perot acoustic sensor based on a photonic-crystal mirror," Meas. Sci. Technol. **18**, 3049 (2007).
24. F. Benabid, J. C. Knight, G. Antonopoulos, *et al.*, "Stimulated Raman scattering in hydrogen-filled hollow-core photonic crystal fiber," Science **298**, 399–402 (2002).
25. J. C. Travers, W. Chang, J. Nold, *et al.*, "Ultrafast nonlinear optics in gas-filled hollow-core photonic crystal fibers," J. Opt. Soc. Am. B **28**, A11–A26 (2011).
26. H. Bao, Y. Hong, W. Jin, *et al.*, "Modeling and performance evaluation of in-line Fabry-Perot photothermal gas sensors with hollow-core optical fibers," Opt. Express **28**, 5423–5435 (2020).
27. W. Jin, Y. Cao, F. Yang, *et al.*, "Ultra-sensitive all-fibre photothermal spectroscopy with large dynamic range," Nat. Commun. **6**, 6767 (2015).
28. P. Zhao, Y. Zhao, H. Bao, *et al.*, "Mode-phase-difference photothermal spectroscopy for gas detection with an anti-resonant hollow-core optical fiber," Nat. Commun. **11**, 847 (2020).
29. R. Dicke, "The effect of collisions upon the Doppler width of spectral lines," Phys. Rev. **89**, 472 (1953).
30. M. B. Marinov, B. Ganev, N. Djermanova, *et al.*, "Analysis of sensors noise performance using Allan deviation," in *IEEE XXVIII International Scientific Conference Electronics (ET)* (IEEE, 2019), pp. 1–4.
31. F. Farahi, P. A. Leilabady, J. Jones, *et al.*, "Interferometric fibre-optic hydrogen sensor," J. Phys. E **20**, 432 (1987).
32. X. Bevenot, A. Trouillet, C. Veillas, *et al.*, "Surface plasmon resonance hydrogen sensor using an optical fibre," Meas. Sci. Technol. **13**, 118 (2001).
33. Y. Oki, S. Nakazono, Y. Nonaka, *et al.*, "Sensitive H_2 detection by use of thermal-lens Raman spectroscopy without a tunable laser," Opt. Lett. **25**, 1040–1042 (2000).
34. S. Hanf, T. Bögözi, R. Keiner, *et al.*, "Fast and highly sensitive fiber-enhanced Raman spectroscopic monitoring of molecular H_2 and CH_4 for

point-of-care diagnosis of malabsorption disorders in exhaled human breath," Anal. Chem. **87**, 982–988 (2015).
35. F. Yang and W. Jin, "All-fiber hydrogen sensor based on stimulated Raman gain spectroscopy with a 1550 nm hollow-core fiber," in *25th Optical Fiber Sensors Conference (OFS)* (IEEE, 2017), pp. 1–4.
36. T. Liang, S. Qiao, X. Liu, *et al.*, "Highly sensitive hydrogen sensing based on tunable diode laser absorption spectroscopy with a 2.1 μm diode laser," Chemosensors **10**, 321 (2022).
37. S.-I. Zaitsu and T. Imasaka, "Intracavity phase-matched coherent anti-Stokes Raman spectroscopy for trace gas detection," Anal. Sci. **30**, 75–79 (2014).
38. Y. Hong, F. Chen, H. Bao, *et al.*, "Amplified photothermal phase modulation for carbon dioxide detection by operating a dual-mode interferometer at destructive interference," Anal. Chem. **95**, 4204–4211 (2023).
39. G. Gagliardi, M. Salza, S. Avino, *et al.*, "Probing the ultimate limit of fiber-optic strain sensing," Science **330**, 1081–1084 (2010).
40. R. Pennetta, M. T. Enders, M. H. Frosz, *et al.*, "Fabrication and non-destructive characterization of tapered single-ring hollow-core photonic crystal fiber," APL Photon. **4**, 056105 (2019).
41. P. Zhao, H. L. Ho, W. Jin, *et al.*, "Gas sensing with mode-phase-difference photothermal spectroscopy assisted by a long period grating in a dual-mode negative-curvature hollow-core optical fiber," Opt. Lett. **45**, 5660–5663 (2020).
42. Y. Lin, W. Jin, F. Yang, *et al.*, "Pulsed photothermal interferometry for spectroscopic gas detection with hollow-core optical fibre," Sci. Rep. **6**, 39410 (2016).
43. M. Michieletto, J. K. Lyngsø, C. Jakobsen, *et al.*, "Hollow-core fibers for high power pulse delivery," Opt. Express **24**, 7103–7119 (2016).
44. A. Vasiliev, A. Malik, M. Muneeb, *et al.*, "On-chip mid-infrared photothermal spectroscopy using suspended silicon-on-insulator microring resonators," ACS Sens. **1**, 1301–1307 (2016).
45. Y. Qi, F. Yang, Y. Lin, *et al.*, "Nanowaveguide enhanced photothermal interferometry spectroscopy," J. Lightwave Technol. **35**, 5267–5275 (2017).
46. R. J. Clark and T. J. Dines, "Resonance Raman spectroscopy, and its application to inorganic chemistry. New analytical methods (27)," Angew. Chem. (Int. Ed. Engl.) **25**, 131–158 (1986).
47. I. Pockrand, *Surface Enhanced Raman Vibrational Studies at Solid Gas Interfaces* (Springer, 2006).
48. H. Liao and Y. Zhao, "Stimulated Raman photothermal spectroscopy for gas sensing in a hollow-core optical fiber [Data set]," Zenodo, 2024, https://doi.org/10.5281/zenodo.14168900.